J Mater Sci: Mater Med (2010) 21:2151–2163
DOI 10.1007/s10856-010-4070-0

Biocorrosion properties and blood and cell compatibility of pure iron as a biodegradable biomaterial

Erlin Zhang · Haiyan Chen · Feng Shen

Received: 14 August 2009 / Accepted: 22 March 2010 / Published online: 16 April 2010

Abstract Biocorrosion properties and blood- and cell compatibility of pure iron were studied in comparison with 316L stainless steel and Mg–Mn–Zn magnesium alloy to reveal the possibility of pure iron as a biodegradable biomaterial. Both electrochemical and weight loss tests showed that pure iron showed a relatively high corrosion rate at the first several days and then decreased to a low level during the following immersion due to the formation of phosphates on the surface. However, the corrosion of pure iron did not cause significant increase in pH value to the solution. In comparison with 316L and Mg–Mn–Zn alloy, the pure iron exhibited biodegradable property in a moderate corrosion rate. Pure iron possessed similar dynamic blood clotting time, prothrombin time and plasma recalcification time to 316L and Mg–Mn–Zn alloy, but a lower hemolysis ratio and a significant lower number density of adhered platelets. MTT results revealed that the extract except the one with 25% 24 h extract actually displayed toxicity to cells and the toxicity increased with the increasing of the iron ion concentration and the incubation time. It was thought there should be an iron ion concentration threshold in the effect of iron ion on the cell toxicity.

E. Zhang (✉) · H. Chen
Institute of Metal Research, Chinese Academy of Sciences,
Shenyang 110016, China
e-mail: zhangerlin2009@163.com

H. Chen
Graduate University of Chinese Academy of Sciences,
Beijing 100049, China

F. Shen
School of Materials Science and Engineering, Harbin Institute
of Technology, Harbin 150001, China

1 Introduction

Biomaterials become more and more diversified with the developing of medical science. During 1960s and 1970s, the first generation of biomaterials was developed for use inside human body, of which common feature was their biological inertness [1]. The goal of all first-generation biomaterials was to "achieve a suitable combination of physical properties to match those of the replaced tissue with a minimal toxic response in the host" [2]. By the mid-1980s, the field of biomaterials began to shift in emphasis from achieving exclusively a bioinert tissue response to producing bioactive components that could elicit a controlled action and reaction in the physiological environment [3]. Second-generation biomaterials were designed to be either resorbable or bioactive. Third-generation biomaterials combined properties of bioactive materials and resorbable materials: bioactive materials were made resorbable and resorbable materials were made bioactive [1].

It still has a long way to apply third-generation biomaterials to clinical therapy. Searching for new second-generation biomaterials is suitable to the occasion. Compared with the first-generation inert biomaterials, such as stainless steel and titanium [4], the second-generation resorbable biomaterials will not cause permanent physical irritation or chronic inflammatory discomfort [5]. Currently, the resorbable biomaterials are mainly made of polymers, such as poly lactic acid [6], poly-L-lactic acid [7, 8], collagen [9] and poly-lactic-glycolic acid [7, 10]. However, these polymer based implants usually have an unsatisfactory mechanical strength.

Magnesium alloys show exciting potential as biomedical implants based on the biodegradability and biocompatibility [11, 12]. Moreover, magnesium ion is essential to human metabolism and is naturally found in bone tissue

Table 1 Summary of the mechanical properties of various materials and natural bone [6, 12–20]

Materials	Young's modulus (GPa)	Ultimate tensile strength (MPa)	Fracture toughness (MPam$^{1/2}$)	Elongation (%)	Hardness
Stainless steel	189–205	620–695	50–200	40–52	320–350 HB
Titanium alloy	55–117	758–1200	55–115	10–33	241–375 HB
Magnesium alloy	41–45	65–258	15–40	3–13	57–69 HV
Polymer (PLA)	1.6–2.4	60–65	–	8.5–9.3	17–19 HV
Pure iron	205	245	–	50	80 HB
Synthetic hydroxyapatite	60–117	600	0.35-0.7	0	–
Natural cortical bone	3–30	130–180	3–6	–	–

[13]. However, it was found that magnesium alloys corroded too rapidly, especially in electrolytic, aqueous environments, resulting in subcutaneous gas bubbles, hemolysis and alkalization of body fluid which limited their clinical applications [5]. In addition, low strength and hardness also limit their application as bone screw and bone plate. Table 1 lists the mechanical properties of several biomaterials as well as magnesium alloys and pure iron for comparison.

Pure iron is also corrodible in salt containing fluid. Compared with magnesium alloys, pure iron shows slow corrosion rate, high fracture strength and high hardness. In addition, the reaction products of pure iron in physical environment does not release gas or cause alkalization of body fluid. The average content of iron in human body is approximately 35–45 mg/kg body weight in adult women and men, respectively [21, 22]. In healthy adults, iron loss due to excretion is balanced by absorption of sufficient dietary iron, from 1 to 2 mg daily, to maintain a relatively constant amount of body iron throughout lift [21, 22]. Being one of the most abundant elements in the human body, iron plays important roles in cellular processes such as the synthesis of DNA, RNA and proteins, electron transport, cellular respiration, cell proliferation and differentiation, and regulation of gene expression [21, 23–25]. Most importantly, iron deficiency is a worldwide problem although it plays a crucial role in health. A report from the World Health Organization (WHO) estimates that 46% of 5–14 year-old children in world are anemic [26]. Physiological iron loss from the body includes the excretion of iron in bile, urine iron, and the daily loss of cells from the skin and gut [21]. Iron metabolism takes place in specialized tissues: testes, brain, intestines, placenta, and skeletal muscle [14]. As iron deficiency affects human health [15], iron overload also lead to many diseases [16]. The capacity of excreting iron through excretion and sloughing of cells from skin and mucosal surfaces is very limited [27] and thus iron homeostasis requires tight regulation, otherwise cellular iron overload leads to toxicity and cell death via free radical formation and lipid peroxidation [28, 29].

Recently, pure iron was studied as biodegradable stent materials in vivo [30]. Short-term effects of the biodegradable iron stent in porcine coronary arteries demonstrated that iron stent was safe and did not show evidence of stent particle embolization or thrombosis and traces of excess inflammation, or fibrin deposition [31]. Long-term effects also demonstrated that there were no signs of local or systemic toxicity [32] and significant obstruction of the stented vessel caused by inflammation, neointimal proliferation, or thrombotic events [33]. However, little fundamental information on the biocorrosion and blood compatibility of pure iron was reported so far. In this paper, in vitro experiments were conducted on pure iron in order to reveal the biocorrosion and blood compatibility of pure iron as a biodegradable implant material.

2 Experimental

2.1 Sample preparation

A pure iron bar with a purity of 99.9 wt% was used. Samples with a dimension of 10 mm × 10 mm × 10 mm for electrochemical test and samples with a dimension of 10 mm × 10 mm × 2 mm for immersion test and blood and cell test were cut from the bar directly, and mounted by epoxy resins with an exposed area of 1 cm^2. The surface was ground by 240–1200 # SiC papers followed by a polishing up to 1 μm. In some tests, magnesium alloy (Mg–1.10Mn–1.05Zn, wt% [34]) and 316L stainless steel were also used for comparison.

2.2 Biocorrosion testing

2.2.1 *Electrochemical test*

All electrochemical tests were carried out at 37 ± 1°C in a beaker containing 350 ml of Hank's solution on a PARSTAT 2273 automatic laboratory corrosion measurement system using a standard three-electrode configuration: the saturated calomel as a reference, a platinum electrode as the counter and the sample as the working electrode. In the open circuit potential-time tests, the working electrode was used to measure OCP up to 3600 s. In the potentiodynamic polarization tests, the working electrode was first immersed in Hank's solution for 20 min and then the polarization curve was measured at a scanning rate of 0.5 mV/s. In order to ensure the results are not due to electrode fouling, the electrode was cleaned by 5000 # SiC papers after each measurement.

2.2.2 *Immersion test*

Immersion tests were carried out in Hank's solution according to ASTM-G31-72 [35]. Samples were immersed in 150 ml solution at 37°C for 7, 14, 21 and 28 days, respectively. Then the samples were removed from Hank's solution, gently rinsed with distilled water and absolute alcohol, and dried at room temperature. After that, samples were cleaned using a solution [36] of 595 g/l hydrochloric acid and 3.5 g/l hexamethylene tetramine to remove the surface corrosion products, and rinsed with alcohol, dried at room temperature and finally weighed to calculate the weight loss and the weight loss rate: weight loss = (weight before immersion − weight after clean)/surface area, weight loss rate = (weight before immersion − weight after clean)/(surface area × immersion time). The sample weight was measured before and after immersion by a balance with an accuracy of 0.1 mg. Morphologies, microstructures and surface chemical composition of the immersed sample were characterized by scanning electron microscope (SEM, SSX-550, Shimadzu Corp.), equipped with energy-disperse spectrometer (EDS); X-ray diffractometer (XRD, D/MAX-RB, Rigaku Corporation) and X-ray photoelectrons spectroscopy (XPS, Escalab250, Thermo Corporation). pH value of Hank's solution with and without iron samples was recorded against time by a pH meter with an accuracy of 0.001. An average of three measurements was taken for each group.

2.3 Blood compatibility

2.3.1 *Hemolysis assay [37]*

Fresh whole blood from a healthy rabbit containing sodium citrate (3.8 wt%) in a ratio of 9:1 was diluted with normal saline (8 ml fresh rabbit blood was diluted by addition of 10 ml normal saline). Pure iron samples were rinsed three times with deionized water and normal saline, and then dipped in a standard tube containing 10 ml of normal saline that was previously incubated at 37°C for 30 min. Then 0.2 ml of diluted blood was added to the tube and the mixture was incubated at 37°C for 60 min. Normal saline solution was used as a negative control and deionized water as a positive control. After this, all tubes were centrifuged at 3000 rpm for 5 min and transferred to cuvettes for optical density measurement at a wavelength of 545 nm by an enzyme-linked immunoassay (ELISA) reader. The hemolysis ratio (HR) was calculated by

$$\mathrm{HR}(\%) = \frac{O.D.(test) - O.D.(negative\ control)}{O.D.(positive\ control) - O.D.(negative\ control)} \times 100\%$$

where O.D.(test), O.D.(positive control) and O.D.(negative control) are the optical densities of the test sample, the positive control and the negative control, respectively. All date were calculated based on the average of three replicates.

2.3.2 *Dynamic clotting time*

All samples, including pure iron, magnesium alloy and 316L stainless steel, were disinfected with ultraviolet ray for 30 min. The examples were placed in a incubator at 37°C for 5 min and 100 µl rabbit whole blood (containing 3.8 wt% citrate acid solution, blood/citrate acid = 9:1) was dropped onto the surface of the examples, followed by the addition of 10 µl of 0.2 mol/l $CaCl_2$ solution and mixed uniformly. After 10, 30, 50, 70 and 90 min, each sample was transferred into a beaker containing 50 ml of distilled water and rinsed gently, then the optical density of the supernatant was determined at 545 nm wavelengths using a spectrophotometer. The relationship between the optical density and time was plotted as the clotting time curve, which would indicate the relative clotting time of each sample. The initial clotting time and the whole clotting time were defined as a time interval when the optical density of solution is 0.1 and 0.01, respectively.

2.3.3 *Prothrombin time (PT)*

Prothrombin time was measured to assess hylan-induced deferment or interdiction of the extrinsic coagulation pathway. Platelet poor plasma (PPP) was prepared by centrifuging the whole blood (containing 3.8 wt% citrate acid solution, blood/citrate acid = 9:1) extracted from a healthy rabbit at 3000 rpm for 15 min. Samples were rinsed with distilled water for 10 min and then dried at room temperature followed by disinfection with ultraviolet ray for 30 min. Hundred and fifty microliter PPP was dropped onto the surface of the sample and then incubated at 37°C for 3 min. Afterwards 100 µl incubated PPP solution was added into 200 µl PT reagent (PT reagent kit, Wuhan Zhongtai Biotech) in a test tube. Immediately, the time for initiation of the first fibrin strand formation was detected automatically by the semi-automatic coagulation instrument (GF-2000IIsemi-automatic coagulation instrument, Shandong Gaomi Caihong).

2.3.4 *Plasma recalcification time (PRT)*

Plasma recalcification time was measured to compare substrate-induced delay in clotting or PPP following activation of prothrombin (factor II) in the presence of Ca^{2+}. Platelet rich plasma (PRP) was prepared by centrifuging the whole blood (containing 3.8 wt% citrate acid solution, blood/citrate acid = 9:1) extracted from a healthy rabbit at 1500 rpm for 15 min. Samples were rinsed with distilled water for 10 min and then dried at room temperature followed by disinfection with ultraviolet ray for 30 min. 150 μl PRP was dropped onto the surface of the samples and incubated for 3 min at 37°C. Then the PRT measurements were performed by adding 100 μl incubated PRP solution into 100 μl $CaCl_2$ solution (0.025 mol/l) incubated in a test tube at 37°C for 30 min. Immediately, the time for initiation of the first fibrin strand formation was detected automatically by the semi-automatic coagulation instrument.

2.3.5 *Platelet adhesion*

The PRP was overlaid the samples and incubated at 37°C for 0.5–3 h, respectively. The samples were rinsed with phosphate buffer solution (PBS) to remove the non-adherent platelets. The adhered platelets were fixed in 2.5 vol.% glutaraldehyde solutions for 12 h at room temperature followed by dehydration in a gradient ethanol/distilled water mixture. After dehydrating, the samples were subsequently dealcoholized through 50, 75, 90 and 100% isoamyl acetate water solutions twice for 10 min each and dried at 4°C. The samples were coated by Au and observed under SEM. The photographs of platelets were randomly taken from the observation. Nine of different field were randomly chosen to count the number of platelets and values were expressed as number density of adhered platelets per square millimeter of surface.

2.4 MTT test

Mouse bone marrow stem cells were cultured in the Dulbecco's Modified Eagle's Medium (DMEM, Gibco) with 10% fetal bovine serum (FBS, Gibco), 100 U/ml penicillin and 100 μg/ml streptomycin in a humidified atmosphere of 5% CO_2 at 37°C. The toxicity tests were carried out by indirect contact. Extracts were prepared using DMEM medium as the extraction medium in a humidified atmosphere with 5% CO_2 at 37°C for 24–72 h according to ISO 10993-5 [38] and ISO 10993-12 [39], named 24 h-extract and 72 h-extract, respectively. The ratio of the total surface area of samples to the volume of extraction medium was at 3 cm^2/ml. Extracts were filtrated though bacterial filters to remove particulate matter, then serially diluted to 50–10% concentration. DMEM culture medium was used as negative control. Cells were incubated in 96-well cell culture plates at 1×10^3 cells/100 μl medium in each well and incubated in a humidified atmosphere with 5% CO_2 at 37°C for 24 h. The medium was then replaced with 100 μl corresponding extracts. After being incubated in a humidified atmosphere with 5% CO_2 at 37°C for 2, 4 and 7 days, respectively, the mediums were discarded and replaced by 20 μl MTT solution at the end of each incubation time, and then incubated at 37°C for 6 h. Then, the medium was discarded and replaced by 150 μl dimethylsulfoxide (DMSO). After gentle shaking for 10 min, the optical density was determined with an enzyme-linked immunoassay (ELISA) reader at a wavelength of 545 nm. All experiments were carried out in triplicate. The cell viability was expressed as "Relative Growth Rate" (RGR) determined by

$$\mathrm{RGR}(\%) = \frac{O.D.(test)}{O.D.(negative\ control)} \times 100\%$$

where O.D.(test) and O.D.(negative control) are the optical densities of the testing sample and the negative control, respectively. The data was expressed in mean ± S.D.

2.5 Statistical analysis

All data were expressed as mean ± standard deviation. Differences between two groups were analyzed by the independent-samples *t*-test. A value of $p < 0.05$ was considered to be statistically significant.

3 Results

3.1 Biocorrosion properties

Figure 1a shows the OCP—time curve of the pure iron sample in Hank's solution. OCP decreased as the time increasing. Figure 1b shows the polarization curve of the pure iron. No plateau can be found in the anodic region, showing that no passivation film was formed on the surface of the pure iron to protect the sample from corrosion attack. Table 2 lists the electrochemical parameters of the pure iron obtained from Fig. 1b. The electrochemical parameters of Mg–Zn–Mn alloy and 316L in Hank's solution are also listed for comparison. The highest corrosion potential (E_{corr}) together with the highest break potential (E_b) was observed for 316L stainless steel, indicating the corrosion rate of 316L stainless steel is extremely low. E_{corr} and E_b of the pure iron are all lower while the corrosion current (I_{corr}) is higher than those of 316L stainless steel, demonstrating

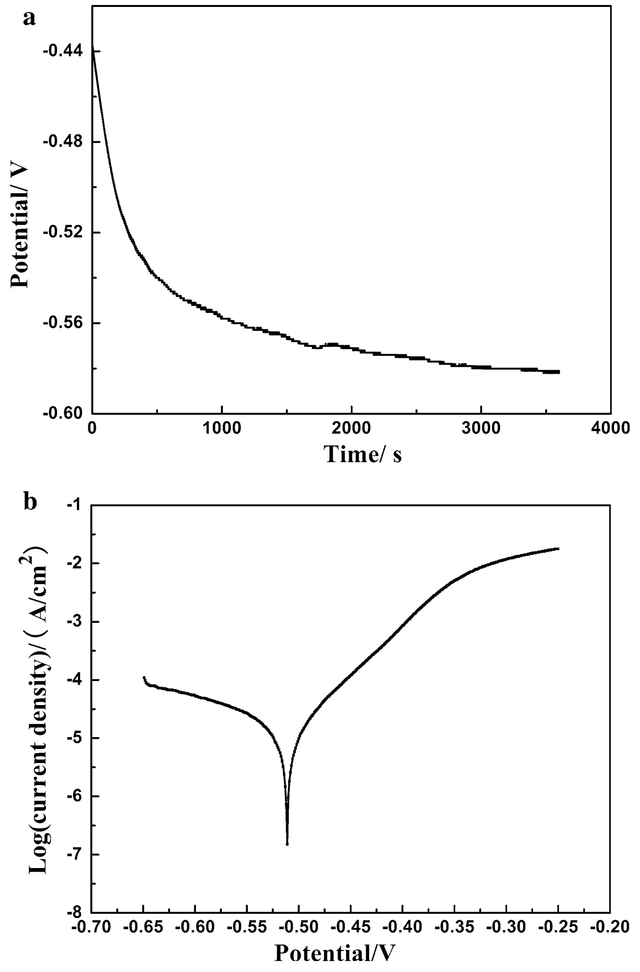

Fig. 1 **a** open circuit potential-time curve, and **b** polarization curve of the pure iron

that the corrosion rate of the pure iron is higher than that of 316L stainless steel. A higher E_{corr} together with a higher E_b but a lower I_{corr} was observed for the pure iron compared with Mg–Mn–Zn alloy, showing that the corrosion rate in Hank's solution of the pure iron is lower than that of Mg–Mn–Zn alloy.

Figure 2 shows the weight loss and the weight loss rate curves of pure iron samples in Hank's solution. The weight loss fast at the first 21 days, however, a low weight loss was observed during the following immersion. Also the weight loss rate kept at a relatively high level at the first 21 days and then decreased to a low level during the following immersion.

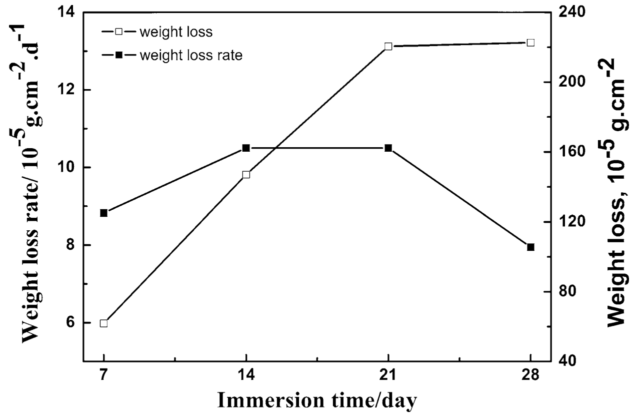

Fig. 2 Weight loss and weight loss rate of pure iron samples in Hank's solution

Figure 3 shows the pH value of Hank's solution with and without the pure iron sample. It was noted that the pH value of Hank's solution without the pure iron sample increased with time, especially in the first 4 days. The pH value of Hank's solution with the pure iron sample exhibited a similar tendency, but the pH value was slightly high. With the consideration of the increase in the pH value of Hank's solution without the pure iron sample, it can be concluded that the increase in the pH value of Hank's solution with the pure iron sample is partly caused by the corrosion of the pure iron sample. An absolute increase in pH value caused by the corrosion of the pure iron sample (the pH of Hank's solution with the pure iron sample — the pH of Hank's solution without the pure iron sample) is in a range of 0–0.26, indicating that the corrosion of the pure iron sample resulted in a limited increase in the pH value.

3.2 Surface microstructure

Figure 4 shows XRD pattern on the pure iron immersed in Hank's solution for 4 weeks. $Mg_3(PO_4)_2$, $Ca_3(PO_4)_2$ and $Fe_3(PO_4)_2{\cdot}8H_2O$ were detected by XRD, indicating that the corrosion products were mainly composed of phosphates. Figure 5a depicts the wide scan XPS spectra of the pure iron immersed in Hank's solution for 4 weeks, with elements Fe, O, P, C, Ca, Mg and Na being detected. All the binding energies were referenced to that of C 1s peak at 284.6 eV. The spectra of Fe 2p is shown in Fig. 5b. After

Table 2 Electrochemical parameters of the pure iron in comparison with Mg–Mn–Zn alloy and 316L stainless steel

Materials	$E_{corr,}$ V	$I_{corr,}$ A	E_b, V	E_b– E_{corr}, V	Ref.
Pure Fe	−0.510	1.68×10^{-5}	−0.40	0.11	This work
Mg–Mn–Zn alloy	−1.505	7.92×10^{-5}	−1.308	0.197	Erlin Zhang [34]
316L stainless steel	−0.246	9.11×10^{-7}	0.‘233	0.479	Kemin Zhang [40]

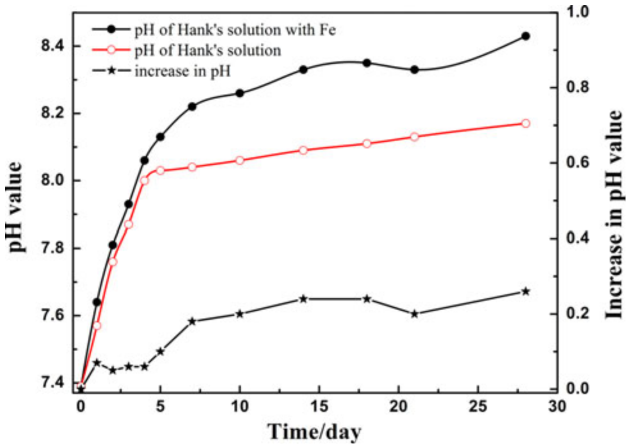

Fig. 3 pH value curves of Hank's solution with and without the pure iron sample and the absolute pH value increase curve of Hank's solution with the pure iron sample

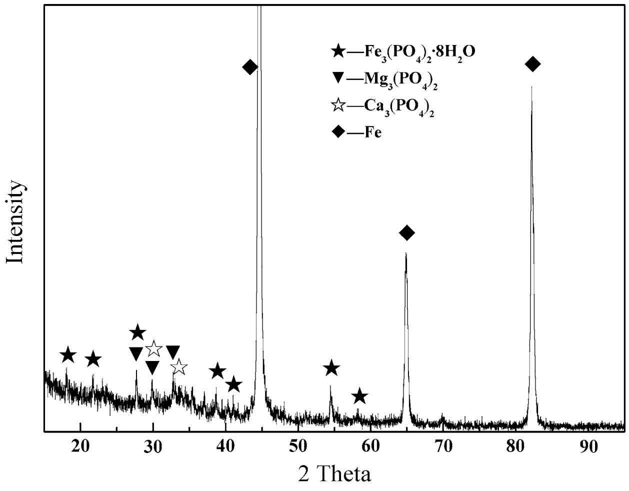

Fig. 4 XRD pattern of the pure iron sample immersed in Hank's solution for 4 weeks

30 s ion etching, no difference was observed in the wide scan spectra and Fe 2p spectra compared with top surface (without ion etching). However, the intensity of Fe 2p was quite weak, which indicates Fe content in the surface products is low. According to Fig. 5b, it is deduced that the element Fe is mainly in the form of Fe^{2+} with small amount of Fe^{3+}.

Figure 6 illustrates the surface microstructure and EDS result of the pure iron immersed in Hank's solution for 4 weeks. Some plate-like crystals and floc were observed on the surface as shown in Fig. 6a. EDS analysis at different location, as shown in Fig. 6b, indicates that the plate-like crystals and floc were mainly composed of C, O, P, Ca and Fe and a small amount of Mg was also detected in the floc. Combined with the XRD and XPS result shown in Figs. 4, 5, it can be concluded that the plate-like crystals were mainly composed of $Ca_3(PO_4)_2$ and $Fe_3(PO_4)_2 \cdot 8H_2O$ while the floc was mainly composed of $Mg_3(PO_4)_2$, $Ca_3(PO_4)_2$ and $Fe_3(PO_4)_2 \cdot 8H_2O$. Figure 7 illustrates the surface topography of the immersed pure iron sample after cleaning. Some corrosion holes were homogeneously distributed on the surface of the sample, meaning that the pure iron sample was corroded in a uniform corrosion mode.

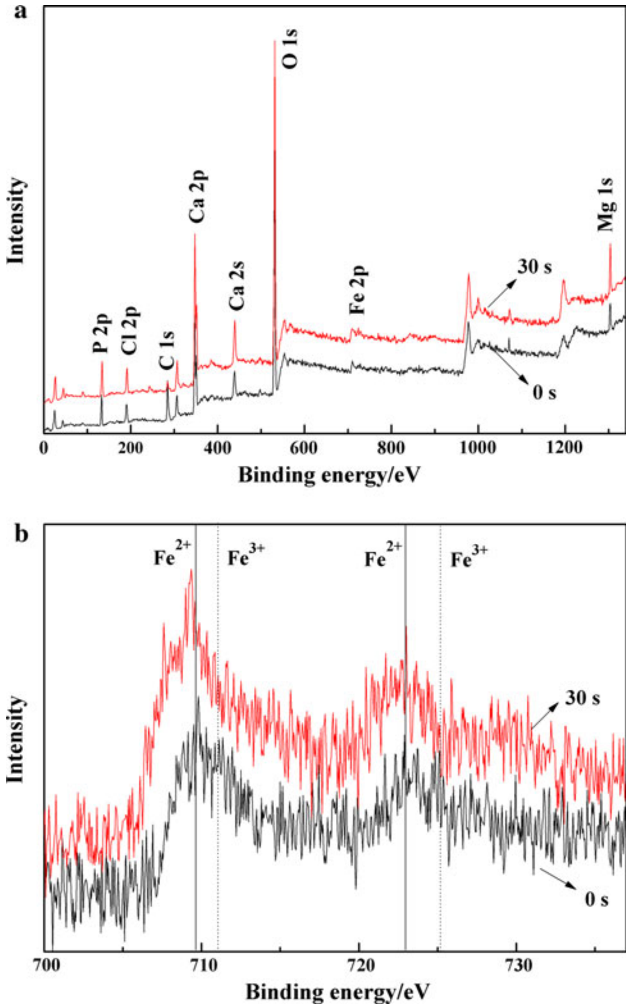

Fig. 5 XPS spectra of the pure iron after immersion in Hank's solution for 4 weeks: **a** wide scan spectra. **b** Fe 2p spectra

3.3 Blood compatibility

3.3.1 Hemolysis

Hemolysis is regarded as an especially significant screening test. A high plasma hemoglobin level normally indicates hemolysis and reflects erythrocyte membrane fragility in contact with materials and devices. Table 3 lists the hemolysis ratio of the pure iron. The results of Mg–Mn–Zn alloy and 316L stainless steel are also listed for comparison. Optical density of the negative control and the positive control both are within the recommended values

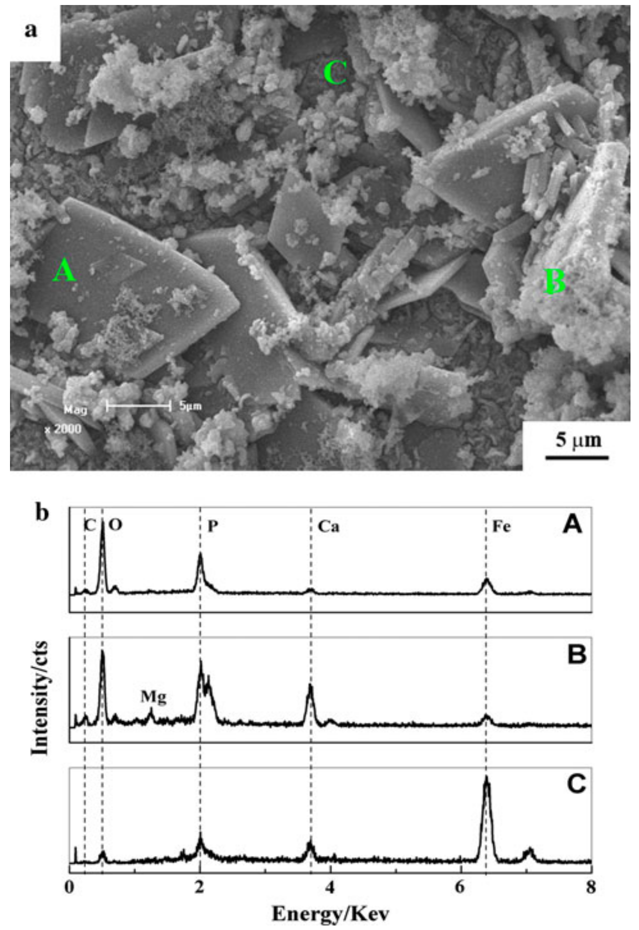

Fig. 6 **a** SEM surface topography of the pure iron sample immersed in Hank's solution for 4 weeks. **b** EDS spectra of location *A*, *B* and *C* in Fig. 6a

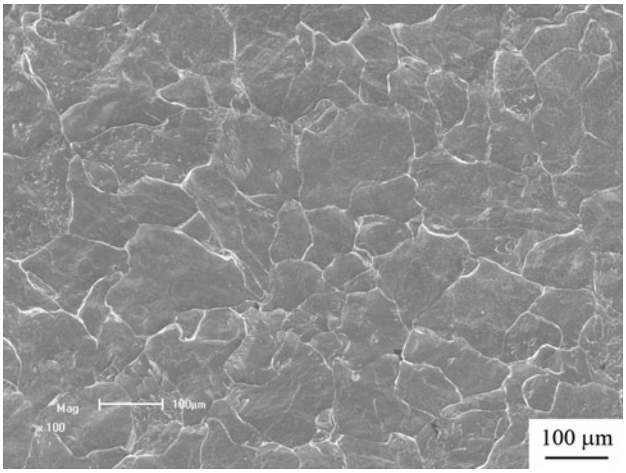

Fig. 7 SEM surface topography of the pure iron sample after cleaning corrosion products

according to ISO 10993-4 [41], respectively. According to the data in Table 3, the hemolysis ratio of pure iron is about 2.44%, lower than the recommended value of 5% in standard ISO 10993-4, indicating that the pure iron does not cause hemolysis to blood system. Compared with Mg–Mn–Zn alloy and 316L stainless steel, the pure iron possesses an excellent anti-hemolysis property.

3.3.2 Dynamic clotting time

In vitro dynamic blood clotting time test measures the degree of intrinsic coagulation factors activation when tested materials are contacted with blood. Figure 8 shows the dynamic clotting time curve of the pure iron. The dynamic clotting time curve of the pure iron decreased smoothly with an increase in time. The initial clotting time and the whole clotting time were calculated from Fig. 8 and listed in Table 4. The results of Mg–Mn–Zn alloy and 316L stainless steel are also listed for comparison. The initial clotting time and the whole clotting time of three kinds of materials are in the same level, and the initial clotting time of pure iron was slightly longer than that of 316L stainless steel, demonstrating the pure iron as well as stainless steel and Mg–Mn–Zn alloy possesses outstanding anticoagulant property.

3.3.3 PT and PRT

Table 3 shows PT and PRT values of the pure iron. The values of 316L stainless steel and Mg–Mn–Zn alloy are also measured and listed for comparison. For PT value, there is a significant difference ($p = 0.002 < 0.05$) between the pure iron and Mg–Mn–Zn alloy, but no difference ($p = 0.568$) between the pure iron and 316L stainless steel. For PRT value, there is also a significant difference ($p = 0.024 < 0.05$) between the pure iron and Mg–Mn–Zn alloy, but no difference ($p = 0.261$) between the pure iron and 316L stainless steel. The PT of the pure iron is similar to that of 316L stainless steel, but the PRT of the pure iron is slightly less than that of 316L stainless steel and Mg–Mn–Zn alloy, indicating the pure iron did not cause obvious effect on the extrinsic coagulation pathway and the intrinsic coagulation pathway.

3.3.4 Platelet adhesion

Figures 9, 10 illustrate the morphologies of platelets on the surfaces of the pure iron, 316L stainless steel and Mg–Mn–Zn alloy after incubation for 0.5–3 h, respectively. After 0.5 h incubation, some platelets on the surface of the pure iron presented round shape and a few was agglomerated and distorted, as shown in Fig. 9a, while the platelets on the surface of 316L stainless steel and Mg–Mn–Zn alloy have extended pseudopodia, as shown in Fig. 9b, c. When the incubation time extended to 3 h, the platelets on the surface of the pure iron presented round approximately

Table 3 HR, PT, PRT, initial and whole clotting time of the pure iron, Mg–Mn–Zn alloy and 316L stainless steel

Materials	Pure iron	Mg–Mn–Zn alloy	316L
HR (%)	2.44	65.75 [34]	5.03 [42]
PT/s	9.6 ± 0.4	7.65 ± 0.25	9.4 ± 0.4
PRT/s	317.4 ± 7.8	341.7 ± 9.1	329.2 ± 13.6
Initial clotting time/min	44	45	39 [43]
Whole clotting time/min	>90	>90	>90 [43]

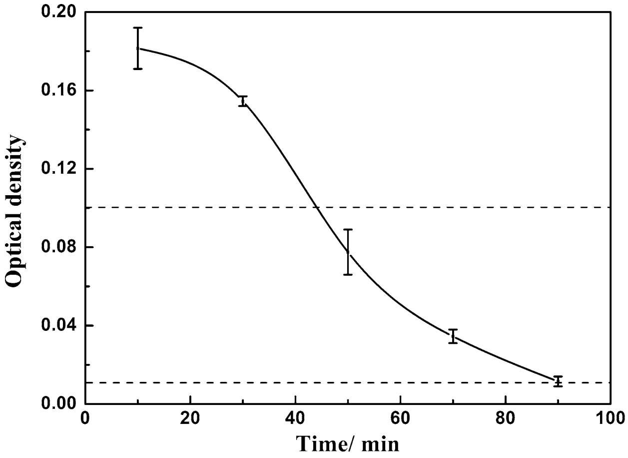

Fig. 8 Dynamic clotting time curve of the pure iron

Table 4 Number densities of platelets on the surface of the pure iron, 316L stainless steel and Mg–Mn–Zn alloy

Incubation period	Pure iron	316L	Mg–Mn–Zn alloy
0.5 h	655 ± 75	4807 ± 350	3715 ± 393
3 h	940 ± 164	7211 ± 633	10270 ± 918

with some short pseudopodia spreading on the surface, as shown in Fig. 10a, while the platelets on 316L stainless steel and Mg–Mn–Zn alloy had many extended pseudopodia and even were activated to interconnection.

Table 4 lists the number density of platelets on the surfaces of the pure iron, 316L stainless steel and Mg–Mn–Zn alloy. There is a significant difference in the number density of platelets on the pure iron and 316L stainless steel ($p < 0.001$), and Mg–Mn–Zn alloy ($p < 0.001$). When the incubation time extended to 3 h, the number density of platelets on the pure iron is still significantly less than that on 316L stainless steel ($p < 0.001$) and Mg–Mn–Zn alloy ($p < 0.001$). This means that the pure iron exhibits very good anti-platelet adhesion properties.

3.4 Cells toxicity

Cell toxicity test was carried out through evaluating the cell viability. Figure 11 illustrates the cell viability cultured in the extracts with 100, 50 and 25% concentration for 2, 4 and 7 days. For all extracts, there is a significant decrease ($p < 0.05$) in the cells viability between all time intervals except for the extract with 100% of 24 h-extract

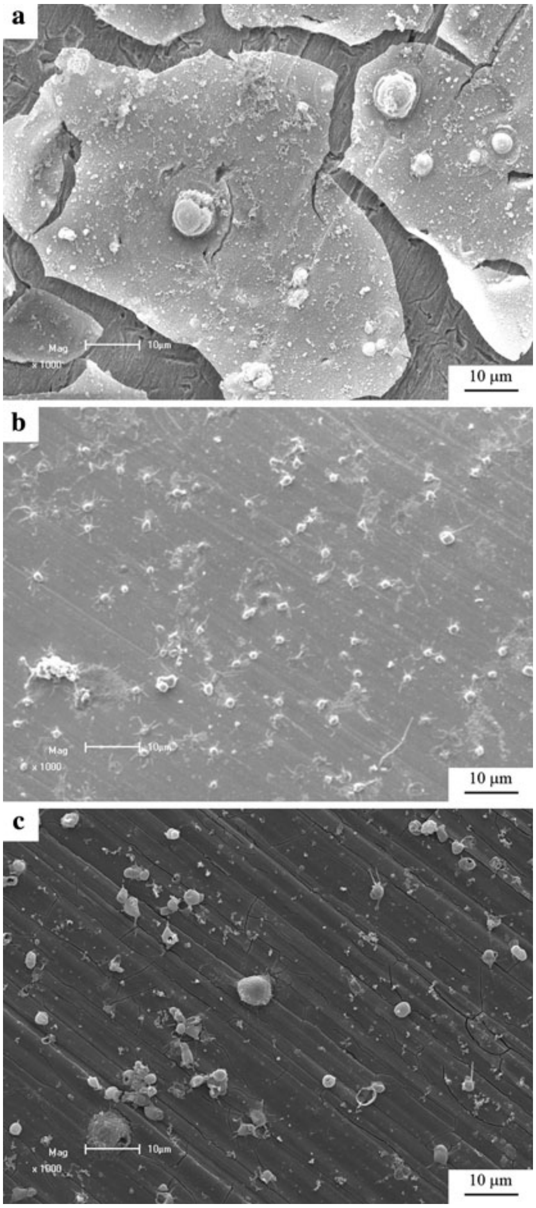

Fig. 9 Platelets on the surface of the pure iron, 316L stainless steel and Mg–Mn–Zn alloy incubated for 0.5 h: **a** pure iron, **b** 316L stainless steel, and **c** Mg–Mn–Zn alloy

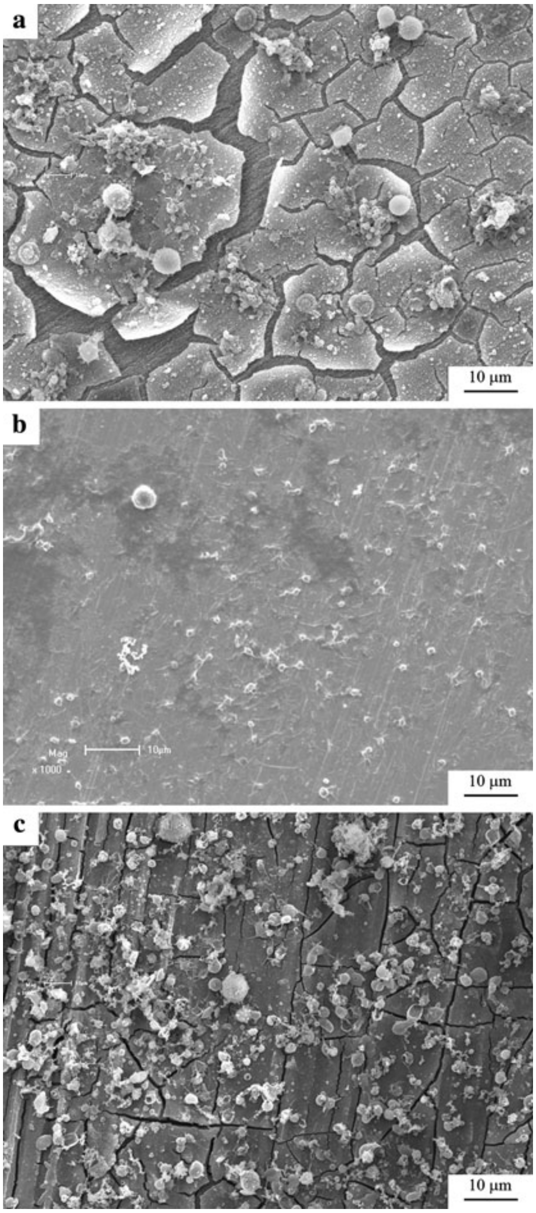

Fig. 10 Platelets on the surface of the pure iron, 316L stainless steel and Mg dipped in the fresh rabbit blood plasma for 3 h: **a** pure iron, **b** 316L stainless steel, and **c** Mg–Mn–Zn alloy

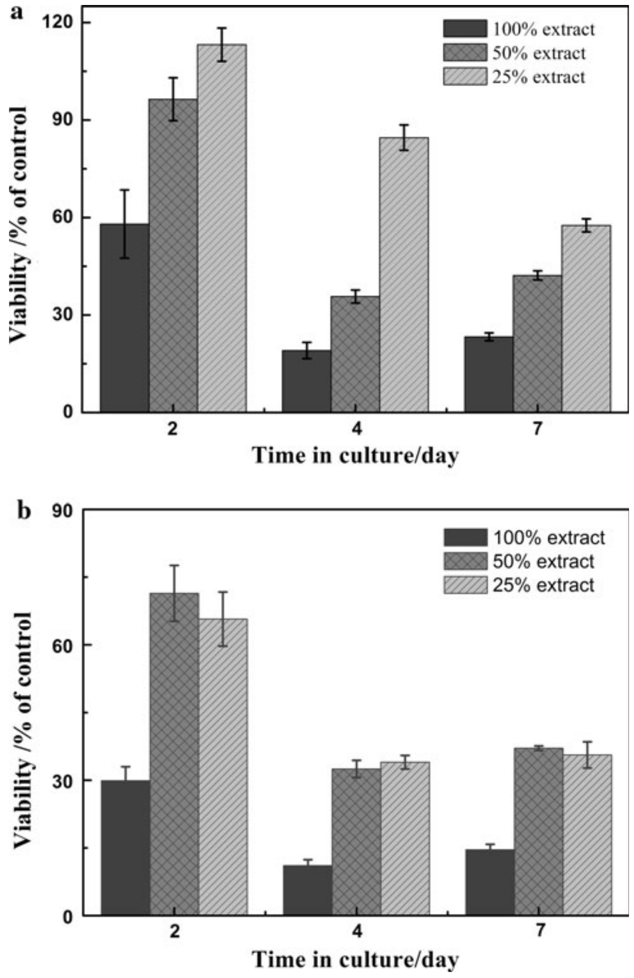

Fig. 11 Cells viability after 2, 4 and 7 days of culture in the extract media with 100, 50 and 25% concentration, respectively. **a** 24 h-extract. **b** 72 h-extract

($p = 0.078$) and the extract with 25% of the 72 h-extract ($p = 0.471$) between 4–7 days. For 24 h-extract, as shown in Fig. 11a, the cells viability decreased obviously ($p < 0.05$) with the increasing of extract concentration. Similar result was observed for the case of 72 h-extract, but no significant difference is found between the extract with 50% of the 72 h-extract and the extract with 25% of the 72 h-extract at day 2 ($p = 0.358$), day 4 ($p = 0.402$) and day 7 ($p = 0.462$). In comparison with the 24 h-extracts with different concentration, the cells viability cultured in the 72 h-extracts with the same concentration showed a statistically significant decrease ($p < 0.05$) except for the concentration of 50% ($p = 0.135$) at all incubation time. Therefore, it is concluded that cells viability is positively influenced by the iron ion concentration and the incubation time. According to Fig. 11, it can also be seen that cells cultured in the extracts with 25% of the 24 h-extract showed a higher optical density than the control at day 2, indicating that the extract with 25% of the 24 h-extract caused no influence on cells proliferation after 2 days incubation, while other extracts exhibited toxicity to cells.

4 Discussion

4.1 Biocorrosion properties

As a biodegradable material, the corrosion property is very crucial. The overall degradation way for polymer biomaterials and the rapid corrosion rate for magnesium biomaterials result in the lose of the mechanical strength of the implants before the recovery or healing of the surgical region [5]. Therefore, it is desired that once a biodegradable biomaterial is implanted in human body, it could gradually be dissolved and absorbed in a suitable rate, which matches the recovery or healing rate of the replaced tissue.

In general, the lower OCP is, the higher the corrosion driving force is. Previous study shows that OCP of magnesium alloys increases with time, indicating the corrosion rate of magnesium alloys decrease with time due to the increase in pH value and the accumulation of products on the surface [44]. Electrochemical test in Fig. 1a clearly indicated OCP of the pure iron decreased with the increasing of time in Hank's solution, displaying that the corrosion rate of the pure iron should increase with the increasing of immersion time in Hank's solution, and then get a steady value due to the accumulation of products on the surface. No passivation stage and noble breakdown potential were found in the polarization curve of pure iron, indicating that no protective film formed on the surface of the pure iron during the early stage of corrosion.

The electrochemical results in Table 2 clearly demonstrate that the corrosion rate of the pure iron in Hank's solution is two orders of magnitude higher than that of 316L stainless steel, but lower than that of Mg–Mn–Zn alloy. 316L stainless steel is widely accepted as non-biodegradable and inert biomaterials and the degradation of magnesium alloy is considered to be too fast as implant materials. According to the previous studies [45] on immersion result of Mg–Mn–Zn alloys suggest that the corrosion rate of Mg–Mn–Zn alloys in Hank's solution is one order of magnitude higher than that of pure iron. Therefore, the moderate corrosion rate of the pure iron might meet the requirement as a biodegradable implant material. Immersion result illustrates the weight lost fast at the first 21 days as shown in Fig. 2. However, a steady weight loss was observed during the following immersion while the weight loss rate kept at a relatively high level at the first 21 days and then decreased to a low level during the following immersion. The long-term corrosion rate that increased first and then decreased as shown in Fig. 2 was consistent with the electrochemical results. A paper [46] on phosphating treatment applied to Mg–Mn–Zn alloy suggested the phosphate layer could protect magnesium alloy from fast corrosion. Similarly, the phosphate layer on steel decreased the corrosion rate [47]. According to corrosion products on iron in immersion test, it could be concluded that the decrease of weight loss rate should be affected by the deposition of products mainly composed of phosphates.

Previous studies [48, 49] on the corrosion behavior of pure iron in sea water have shown that pure iron was corroded in a oxygen-absorption corrosion mode.

$$\text{Cathode reaction: } O_2 + 2H_2O + 4e^- = 4OH^- \quad (1)$$

$$\text{Anode reaction: } Fe + 2OH^- - 2e^- = Fe(OH)_2 \quad (2)$$

However, only phosphates including $Mg_3(PO_4)_2$, $Ca_3(PO_4)_2$ and $Fe_3(PO_4)_2{\cdot}8H_2O$ were detected by XRD on the pure iron sample when the sample was immersed in Hank's solution for 4 weeks, as shown in Fig. 4. Hank's solution is a chlorides, sulphate and phosphates containing solution, and the increase in pH value due to the corrosion of the pure iron promotes the precipitation and deposition of phosphates, including $Mg_3(PO_4)_2$, $Ca_3(PO_4)_2$ and $Fe_3(PO_4)_2{\cdot}8H_2O$. Therefore, it is proposed that following reactions happen on the surface of the pure iron and in the solution during the immersion in Hank's solution:

$$Fe(OH)_2 + Cl^- = FeClOH + OH^- \quad (3)$$

$$FeClOH + H^+ = Fe^{2+} + Cl^- + H_2O \quad (4)$$

$$Fe^{2+} + O_2 + 3OH^- = Fe(OH)_3\downarrow + O_2^- \quad (5)$$

$$Fe(OH)_3 + 2Cl^- = FeCl_2OH + 2OH^- \quad (6)$$

$$FeCl_2OH + H^+ = Fe^{3+} + 2Cl^- + H_2O \quad (7)$$

$$2PO_4^{3-} + 3Ca^{2+} = Ca_3(PO_4)_2\downarrow \quad (8)$$

$$2PO_4^{3-} + 3Mg^{2+} = Mg_3(PO_4)_2\downarrow \quad (9)$$

$$2PO_4^{3-} + 3Fe^{2+} + 8H_2O = Fe_3(PO_4)_2{\cdot}8H_2O \quad (10)$$

$$PO_4^{3-} + Fe^{3+} = FePO_4\downarrow \quad (11)$$

The alkalization effect is a severe problem for biodegradable materials such as magnesium alloys [5]. A study by Song, G. L. showed that the corrosion of magnesium implant gave rise to an increase in pH value of local body fluid in adjacent to the magnesium alloy [5], which could unfavorably affect the pH dependent physiological reaction balances and even lead to an alkaline poisoning effect [50]. The pH measurement in Fig. 3 demonstrates that the corrosion of the pure iron only causes slightly alkalization to Hank's solution, about 0.26-increase, which will not cause damage to local body environment. The immersion test also revealed that the pure iron was corroded in a uniform way, as shown in Fig. 7, suggesting that the implant of the pure iron would not lose function through pitting and could exert all its benefit of mechanical properties.

4.2 Blood compatibility

The materials to be used in contact with blood must possess good blood compatibility, such as low hemolysis ratio, excellent anticoagulant property and outstanding anti-thrombus property. The damage and destructive effect of medical material to the erythrocyte is assessed through hemolysis ratio. According to standard ISO 10993-4, the hemolysis ratio has to be less than 5% [38]. The anticoagulant property of medical materials is evaluated through a series of testing including dynamic clotting time, PT and PRT. Generally, long initial clotting time, whole clotting time, PT and PRT are always desired.

Hemolysis result in Table 3 clearly proves that the hemolysis ratio of pure iron is lower than the recommended value, demonstrating that the pure iron causes no damage to erythrocyte. Previous study on magnesium alloys has revealed that the high hemolysis ratio was caused mainly by the significant increase in pH value rather than the releasing of alloying elements concentration due to the corrosion of magnesium alloys [34]. The pH measurement in Fig. 3 indicates that the corrosion of the pure iron did not cause a significant increase in pH value, which contributes to the low hemolysis.

The blood coagulation pathway is divided into intrinsic pathway and extrinsic pathway [51]. The activation degree of the intrinsic pathway is assessed by dynamic clotting time and PRT, while the activation degree of the extrinsic pathway is assessed through PT [52]. 316L stainless steel is applied as stent materials due to its outstanding blood compatibility. The initial clotting time and the whole clotting time of the pure iron and 316L stainless steel are in the same level as shown in Table 4. PRT results in Table 3 also reveal that the effect of the pure iron on the intrinsic coagulation pathway is approximately similar to that of 316L stainless steel. Similar results are also observed in PT value. From these results, it can be concluded that pure iron possesses outstanding anticoagulation properties as stainless does.

Thrombus is blood clot that forms in blood vessel and platelet adhesion at sites of vascular injury is the key step in thrombus [53, 54]. Therefore, platelets adhesion test can detect the effect on the formation of thrombus when tested materials are in contact with blood. The significantly low number density of the platelets and the round-shape of the platelets on the pure iron indicate that the pure iron possesses excellent anti-platelets adhesion property in comparison with 316L stainless steel and Mg–Mn–Zn alloy.

The low hemolysis ratio, the excellent anticoagulant properties and the outstanding anti-platelets adhesion property suggest the pure iron should be a potential biomaterial to be used in contact with blood.

4.3 Cells toxicity

The cells proliferation results in Fig. 11 clearly show that the pure iron exhibits toxicity to mouse bone marrow stem cell during the tested concentration and duration. It can be also found that the toxicity increased with the increasing of extracts concentration and the incubation time, displaying that cells toxicity is relevant to iron ion concentration.

The delivery of iron to cells involves a number of specialized transport systems and membrane carriers [55]. Ferric iron combines with transferring (Tf) and then integrates with a specific cell surface receptor, transferrins receptor 1 (TfR1) [56, 57]. The Fe_2–Tf–TfR1 complex is internalized by receptor-mediated endocytosis, and the iron is released from Tf through a process that involves acidification of endosomes and likely reduction of the iron via the enzyme Steap3 [56, 58]. Divalent metal ion transporter 1 (DMT1) carries the released iron across the endosomal membrane into the cytoplasm of the cell [59, 60], where it can be utilized for metabolic purposes. Most tissues are able to divest themselves of iron, a process mediated predominantly by the iron transporter ferroportin (FPN) [56].

Iron ion is essential to human health [61], but the deleterious effect of iron on cell culture is relevant to its ability to generate reactive oxygen species via Fenton reaction as followings [23, 62, 63].

$$Fe^{3+} + {}^{\bullet}O_2^{-} \rightarrow Fe^{2+} + O_2 \tag{12}$$

$$Fe^{2+} + H_2O_2 \rightarrow Fe^{3+} + {}^{\bullet}OH + OH^{-} \tag{13}$$

Highly reactive oxygen species (ROS), such as hydroxyl (OH^-) and superoxide radicals ($O_2{}^-$), are highly toxic, owing to their ability to react rapidly with almost every molecule found in living cells. In addition, free iron can react directly with unsaturated fatty acids and induce lipid hydroperoxides to form alkoxyl and/or peroxyl radicals and, in turn, severely impair cellular integrity and cause cell death [64].

Although ROS are damaging, they are also generated during normal metabolism in organelles [56]. As long as iron ion level is well maintained within cells, the body will use a range of defense strategies to protect against excessive ROS accumulation and their effects [56]. Based on the toxicity mechanism and toxicity results in Fig. 11, an important conclusion could be elicited: only when the concentration of iron in cells is accumulated to a limited value, the toxicity of iron will be revealed. Another study [30] has reported that the extract with less than 10 µg/ml iron ion enhanced the metabolic activity of cells and the extract with less than 50 µg/ml iron ion did not display toxicity to cells. Thus, how to detect and confirm the safe value of the iron ion concentration is quite important. The extract with 25% of 24 h-extract exhibited no toxicity after 2 day incubation, but toxicity after 4 days incubation. It is proposed that the safe vale of iron ion concentration is close to the ion concentration of the extract with 25% of 24 h-extraction. According to the result of immersion test, the mean weight loss rate of the pure iron in Hank's solution was about 10×10^{-5} $gcm^{-1}day^{-1}$. Supposed the degradable rate of the pure iron in Hank's solution and DMEM culture medium is equal, the calculated iron ion concentration of the extract with 25% of 24 h-extract was is about 0.075 mg/ml. Thus, the safe concentration of iron should be less than 0.075 mg/ml. It was reported elsewhere that the safe iron ion concentration was about 0.050 mg/ml [30] which is close to the calculated safe concentration in this paper.

5 Conclusion

Pure iron exhibited medium corrosion rate in Hank's solution in comparison with magnesium alloy and stainless steel, but the corrosion caused no alkalinization to Hank's solution. It was revealed that the pure iron possessed a low hemolysis ratio, excellent anticoagulant property and outstanding anti-platelets adhesion property. However, the iron ion actually showed toxicity to cell when the iron ion concentration exceeded a critical value.

Acknowledgments One of the authors (Erlin Zhang) would like to acknowledge the financial support from the Institute of Metal Research (IMR), Chinese Academy of Sciences (CAS), Shenyang Science and Technology Institute (Program No. 1062109-1-100), and Heilongjiang Provincial Nature Science Fund (No. E2007-18).

References

1. Hench LL, Polak JM. Third-generation biomedical materials. Science. 2002;295(5557):1014–7.
2. Hench LL. Biomaterials. Science. 1980;208(4446):826–31.
3. Hench LL, Wilson J. Surface-active biomaterials. Science. 1984;226(4675):630–6.
4. Gristina AG. Biomaterial-centered infection: microbial adhesion versus tissue integration. Science. 1987;237(4822):1588–95.
5. Song GL, Song SZ. A possible biodegradable magnesium implant material. Adv Eng Mater. 2007;9(4):298–302.
6. Yang SL, Wu ZH, Yang W, Yang MB. Thermal and mechanical properties of chemical crosslinked polylactide (PLA). Polym Test. 2008;27(8):957–63.
7. Paragkumar NT, Dellacherie E, Six JL. Surface characteristics of PLA and PLGA films. Appl Surf Sci. 2006;253(5):2758–64.
8. Cai KY, Yao KD, Yang ZM, Li XQ. Surface modification of three-dimensional poly(d, l-lactic acid) scaffolds with baicalin: a histological study. Acta Biomater. 2007;3(4):597–605.
9. Lee CH, Singla A, Lee Y. Biomedical applications of collagen. Int J of Pharm. 2001;221(1–2):1–22.
10. Liu SJ, Chi PS, Lin SS, Ueng SW, Chan EC, Chen JK. Novel solvent-free fabrication of biodegradable poly-lactic-glycolic acid (PLGA) capsules for antibiotics and rhBMP-2 delivery. Int J of Pharm. 2007;330(1–2):45–53.
11. Gu XN, Zheng YF, Cheng Y, Zhong SP, Xi TF. In vitro corrosion and biocompatibility of binary magnesium alloys. Biomaterials. 2009;30(4):484–98.
12. Staiger MP, Pietak AM, Huadmai J, Dias G. Magnesium and its alloys as orthopedic biomaterials: a review. Biomaterials. 2006; 27(9):1728–34.
13. Okuma T. Magnesium and bone strength. Nutrition. 2001;17(7–8):679–80.
14. Saber-Samandari S, Gross KA. Micromechanical properties of single crystal hydroxyapatite by nanoindentation. Acta Biomater. In press. doi: 10.1016/j.actbio.2009.02.009.
15. Rack HJ, Qazi JI. Titanium alloys for biomedical application. Mater Sci Eng: C. 2006;26(8):1269–77.
16. Yang Z, Li JP, Zhang JX, Lorimer GW, Robson J. Review on research and development of magnesium alloys. Acta Metall Sinica. 2008;21(5):313–28.
17. Choi JW, Kong YM, Kim HE, Lee IS. Reinforcement of hydroxyapatite bioceramic by addition of Ni_3Al and Al_2O_3. J Am Ceram Soc. 1998;81(7):1743–8.
18. Hassan SF, Gupta M. Development of a novel magnesium–copper based composite with improved mechanical properties. Mater Res Bull. 2002;37(2):377–89.
19. Cheung HY, Lau KT, Tao XM, Hui D. A potential material for tissue engineering: silkworm silk/PLA biocomposite. Compos Part B: Eng. 2008;39(6):1026–33.
20. Tian WS. A study of pure iron machinability. J Taiyuan Heavy Mach Inst. 1990;2:18–24.
21. Lieu PT, Heiskala M, Peterson PA, Yang Y. The roles of iron in health and disease. Mol Aspects Med. 2001;22(1–2):1–87.
22. Dey A, Mukhopadhyay AK, Gangadharan S, Sinha MK, Basu D, Bandyopadhyay NR. Nanoindentation study of microplasma sprayed hydroxyapatite coating. Ceram Int. 2009;35(6):2295–304.
23. Boldt DH. New perspectives on iron: an introduction. Am J Med Sci. 1999;318(4):207–12.
24. Harhaji L, Vuckovic O, Miljkovic D, Stosic-Grujicic S, Trajkovic V. Iron down-regulates macrophage anti-tumour activity by blocking nitric oxide production. Clin Exp Immunol. 2004;137(1):109–16.
25. Jones DT, Trowbridge IS, Harris AL. Effects of transferrin receptor blockade on cancer cell proliferation and hypoxia-inducible factor function and their differential regulation by ascorbate. Cancer Res. 2006;66(5):2749–56.
26. Arredondo M, Nunez MT. Iron and copper metabolism. Mol Aspects Med. 2005;26:313–27.
27. Siah CW, Trinder D, Olynyk JK. Iron overload. Clin Chim Acta. 2005;358(1–2):24–36.
28. Leonarduzzi G, Scavazza A, Biasi F, Chiarpotto E, Camandola S, Vogl S, et al. The lipid peroxidation end product 4-hydroxy-2, 3-nonenal up-regulates transforming growth factor beta 1 expression in the macrophage lineage: a link between oxidative injury and fibrosclerosis. Faseb J. 1997;11(11):851–7.
29. Eaton JW, Qian MW. Molecular bases of cellular iron toxicity. Free Radic Biol Med. 2002;32(9):833–40.
30. Zhu SF, Huang N, Xu L, Zhang Y, Liu H, Sun H, et al. Biocompatibility of pure iron: in vitro assessment of degradation kinetics and cytotoxicity on endothelial cells. Mater Sci Eng: C. 2009;29(5):1589–92.
31. Waksman R, Pakala R, Baffour R, Seabron R, Hellinga D, Tio FO. Short-term effects of biocorrodible iron stents in porcine coronary arteries. J Interv Cardiol. 2008;21(1):15–20.
32. Peuster M, Hesse C, Schloo T, Fink C, Beerbaum P, von Schnakenburg C. Long-term biocompatibility of a corrodible peripheral iron stent in the porcine descending aorta. Biomaterials. 2006;27(28):4955–62.
33. Peuster M, Wohlsein P, Brugmann M, Ehlerding M, Seidler K, Fink C, et al. A novel approach to temporary stenting: degradable cardiovascular stents produced from corrodible metal—results 6–18 months after implantation into New Zealand white rabbits. Heart. 2001;86(5):563–9.
34. Zhang EL, Yin DS, Xu LP, Yang L, Yang K. Microstructure, mechanical and corrosion properties and biocompatibility of Mg–Zn–Mn alloys for biomedical application. Mater Sci Eng: C. 2009;29(3):987–93.

35. ASTM-G31-72: standard practice for laboratory immersion corrosion testing of metals. Annual book of ASTM standards. Philadelphia, PA, USA: Am Soc Test and Mater. 2004.
36. ISO-8407: corrosion of metals and alloys-removal of corrosion products from corrosion test specimens. International Standard Organization; 1991.
37. Singhal JP, Ray AR. Synthesis of blood compatible polyamide block copolymers. Biomaterials. 2002;23(4):1139–45.
38. ISO-10993–5. Biological evaluation of medical devices—part 5: tests for cytotoxicity: in vitro methods. Arlington: ANSI/AAMI; 1999.
39. ISO-10993–12. Biological evaluation of medical devices—part 12: sample preparation and reference materials. Arlington: ANSI/AAMI; 2002.
40. Zhang KM, Yang DZ, Zou JX, Dong C. Surface modification of 316L stainless steel by high current pulsed electron beam II. Corrosion behaviors in the simulated body fluid. Acta Metall Sinica. 2007;43(1):71–6.
41. ISO-10993–4. Biological evaluation of medical devices—part 4: selection of tests for interactions with blood. Arlington: ANSI/AAMI; 1999.
42. Khan W, Kapoor M, Kumar N. Covalent attachment of proteins to functionalized polypyrrole-coated metallic surfaces for improved biocompatibility. Acta Biomater. 2007;3(4):541–9.
43. Yang HJ, Yang K, Zhang BC. Study of in vitro anticoagulant property of the La added medical 316L stainless steel. Acta Metall Sinica. 2006;42:959–64.
44. Yang L, Zhang EL. Biocorrosion behavior of magnesium alloy in different simulated fluids for biomedical application. Mater Sci Eng: C. 2009;29(5):1691–6.
45. Xu L, Zhang E, Yin D, Zeng S, Yang K. In vitro corrosion behaviour of Mg alloys in a phosphate buffered solution for bone implant application. J Mater Sci. 2008;19(3):1017–25.
46. Xu LP, Zhang EL, Yang K. Phosphating treatment and corrosion properties of Mg–Mn–Zn alloy for biomedical application. J Mater Sci. 2009;20(4):859–67.
47. Li GY, Niu LY, Lian JS, Jiang ZG. A black phosphate coating for C1008 steel. Surf Coat Technol. 2004;176(2):215–21.
48. Xu CC, Yue LJ, Ouyang WZ. Corrosion mechanisms and desalination treatments of nlarine iron artifacts. Sci Conserv Archaeol. 2005;17(3):55–9.
49. Zhang Z, Liang YW. Corrosion behavior of iron in sodium chloride solutions with different pH value. Corros Sci Prot Technol. 2008;20(4):260–4.
50. Song GL. Control of biodegradation of biocompatible magnesium alloys. Corros Sci. 2007;49(4):1696–701.
51. Vogler EA, Siedlecki CA. Contact activation of blood-plasma coagulation. Biomaterials. 2009;30(10):1857–69.
52. Triplett DA. Coagulation and bleeding disorders: review and update. Clin Chem. 2000;46(8B):1260–9.
53. Ouared R, Chopard B, Stahl B, Renacht DA, Yilmaz H, Courbebaisse G. Thrombosis modeling in intracranial aneurysms: a lattice Boltzmann numerical algorithm. Comput Phys Commun. 2008;179(1–3):128–31.
54. Nurden AT. Platelets and tissue remodeling: extending the role of the blood clotting system. Endocrinology. 2007;148(7):3053–5.
55. Yang J, Mori K, Li JY, Barasch J. Iron, lipocalin, and kidney epithelia. Am J Physiol-Ren Physiol. 2003;285(1):9–18.
56. Anderson GJ. Mechanisms of iron loading and toxicity. Am J Hematol. 2007;82(12):1128–31.
57. Crichton RR, Wilmet S, Legssyer R, Ward RJ. Molecular and cellular mechanisms of iron homeostasis and toxicity in mammalian cells. J Inorg Biochem. 2002;91(7):652–67.
58. Lill R, Dutkiewicz R, Elsasser HP, Hausmann A, Netz DJA, Pierik AJ, et al. Mechanisms of iron-sulfur protein maturation in mitochondria, cytosol and nucleus of eukaryotes. Biochim Biophys Acta-Mol Cell Res. 2006;1763(7):652–67.
59. Ma YX, Yeh M, Yeh KY, Glass J. Iron imports. V. transport of iron through the intestinal epithelium. Am J Physiol-Gastroint Liver Physiol. 2006;290(3):417–22.
60. Buckett PD, Wessling-Resnick M. Small molecule inhibitors of divalent metal transporter-1. Am J Physiol-Gastroint Liver Physiol. 2009;296(4):798–804.
61. Binet JL. Human iron metabolism—discussion. Bull Acad Natl Med. 2005;189(8):1647.
62. Hershko C. Mechanism of iron toxicity. Food Nutr Bull. 2007;28(4):500–9.
63. Kolnagou A, Michaelides Y, Kontos C, Kyriacou K, Kontoghiorghes GJ. Myocyte damage and loss of myofibers is the potential mechanism of iron overload toxicity in congestive cardiac failure in thalassemia. Complete reversal of the cardiomyopathy and normalization of iron load by deferiprone. Hemoglobin. 2008;32(1–2):17–28.
64. Britton RS, Leicester KL, Bacon BR. Iron toxicity and chelation therapy. Int J Hematol. 2002;76(3):219–28.